J. Fluid Mech. (1999), *vol.* 393, *pp.* 99–121. Printed in the United Kingdom

History forces and the unsteady wake of a cylinder

By J. R. CHAPLIN

Department of Civil Engineering, City University, London EC1V 0HB, UK

(Received 12 December 1997 and in revised form 11 March 1999)

History forces on a stationary cylinder in arbitrary unsteady rectilinear flow are calculated by means of a model based on the asymptotic properties of the steady-state wake. The results capture many features found in numerical solutions of the Navier–Stokes equation for the same flows, though quantitative agreement deteriorates as the Reynolds number increases over the range 2 to 40. The cases studied are the impulsive start, stop, and reverse, and oscillatory flow.

1. Introduction

In conditions where both drag and inertia forces are important, the in-line loading on a bluff body in unsteady flow can be predicted in general only by numerical modelling or by Morison's equation. The latter (Morison *et al.* 1950) was seen initially as a temporary approximation for wave loading on cylinders, but its robustness and simplicity have given it lasting appeal. It relies on knowledge of appropriate drag and inertia coefficients – on which a considerable volume of data is now available – and the fact that it does not address vortex shedding forces directly is often unimportant. But the implicit assumption that the loading depends only on the instantaneous velocity and acceleration gives rise to other shortcomings, and its empirical success should not be considered a justification for neglecting some interesting and important features of the flow and the loading.

Examples of the limitations of Morison's equation are not difficult to find, and an obvious one is the case of a body brought rapidly from rest to a steady velocity. According to Morison's equation, the loading will at once achieve a steady state as soon as the acceleration of the incident flow ceases. This is clearly not the case in reality, since the flow takes much longer to reach a steady, or quasi-steady, state, and appreciable changes occur in the in-line force until the surrounding fluid has travelled several diameters past the body. Another example is that of a body in a flow that reverses. In this case the incident flow is initially enhanced by the velocity deficit of the old wake, contributing to the well-known sensitivity of Morison force coefficients in harmonic flow to the amplitude and frequency of the motion, or in other words, to the Keulegan–Carpenter number, a parameter that has no obvious counterpart in more general conditions.

A force that is obviously missing in Morison's equation is that associated with the history of the flow. Comments to this effect can be found in the literature from the earliest days of research into problems related to wave loading on cylinders, but very few authors have pursued the subject further than a reference to Basset's (1888) classical result for the history force on a sphere at zero Reynolds number. However, more recently, progress has been made in understanding history forces on

small particles, bubbles and droplets in conditions where the elementary particle can be assumed to be spherical, and Reynolds numbers may be of order 1. The present paper aims to transpose some of these ideas to the analytically much less promising case of two-dimensional flow around a cylinder, for which history forces have received scarcely any previous attention.

2. Previous work and present objectives

The earliest mention of history forces is usually attributed to Basset (1888, vol. 2, p. 291, equation 18), although the same result had been derived earlier by Boussinesq (1885*a*, *b*, see Vojir & Michaelides 1994). The outcome was the same, and is generally, if unfairly, referred to as the Basset history force. When applied to the case of a stationary sphere in a fluid moving with velocity $\boldsymbol{U}(t)$ this results in the following formula for the total force on the sphere:

$$\boldsymbol{F}(t) = 6\pi\mu c\boldsymbol{U}(t) + 2\pi\rho c^3\dot{\boldsymbol{U}}(t) + 6\rho c^2\sqrt{\pi\nu}\int_{-\infty}^{t}\frac{\dot{\boldsymbol{U}}(\tau)}{\sqrt{t-\tau}}\mathrm{d}\tau, \tag{1}$$

where μ is the coefficient of dynamic viscosity, c the sphere's radius, ρ the fluid density and $\nu = \mu/\rho$. The first term represents the linear (Stokes) drag, the second term is the inertia force (corresponding to an added-mass coefficient of $\frac{1}{2}$), and the third term is the history force. The physical meaning of this is that each change in velocity $\dot{\boldsymbol{U}}\mathrm{d}t$ has an effect on the loading that subsequently decays with the inverse square root of time.

Basset's analysis for the force on a sphere neglects convective terms in the equation of motion and is therefore likely to be valid only at small Reynolds numbers. In steady flow, Stokes' law (the first term of (1)) is reasonably accurate up to Reynolds numbers Re of around 1, and to some extent the Oseen approximation $F = 6\pi\mu cU(1 + 3Re/8)$ provides an advance on this by including some features of the convective terms. Steps towards including the convective terms fully were made by Proudman & Pearson (1957), and later Sano (1981) extended their result to the case of a sphere brought impulsively into steady motion from rest. In this case the force approaches its steady value as t^{-2} and not as $t^{-1/2}$ as indicated by (1). Several other types of motion were considered by Lovalenti & Brady (1993), who showed that impulsive starts, stops, reverses, and changes in velocity without reverses all led to history terms with different rates of decay.

In an appendix by Hinch (1993) the form of Lovalenti & Brady's history forces is extracted from much simpler physical concepts related to the overall structure of the flow. This global or asymptotic approach provides a useful reference point for more detailed analyses, and forms one element of a series of papers by Mei, Lawrence & Adrian (1991), Mei (1993, 1994), Lawrence & Mei (1995), Mei & Lawrence (1996), concerned with the flow field and the loading on a sphere in unsteady flow at small Reynolds numbers. Results of numerical solutions of the Navier–Stokes equations were compared with these semi-analytical predictions to show generally good agreement on both flow and forces. The subject is reviewed by Michaelides (1997).

In an experimental test of the Basset history force, Odar & Hamilton (1964) oscillated a sphere in oil initially at rest at Reynolds numbers up to 62. They compared force measurements with a version of Morison's equation that included a

history force term with a new coefficient C_h:

$$F = C_d \tfrac{1}{2}\rho\pi c^2 U|U| + C_a \tfrac{4}{3}\rho\pi c^3 \dot{U} + C_h c^2 \rho\sqrt{\pi\nu}\int_0^t \frac{\dot{U}(\tau)}{\sqrt{t-\tau}}\mathrm{d}\tau. \tag{2}$$

The drag coefficient C_d was taken to be that corresponding to the Reynolds number of the instantaneous velocity, and the other two coefficients were computed by fitting the predicted forces to the measurements and were plotted as functions of the 'acceleration number' $U^2/2c\,\dot{U}$. Some further discussion on the same approach can be found in Hamilton (1972).

The only previous work explicitly on history forces on a cylinder seems to be that by Matsumoto (1996), who derived an approximate linearized general solution for the flow induced by the wake at the cylinder, and from it obtained results for the loading. Predicted velocities and forces were compared with measurements, with rather mixed results. An alternative approach is to analyse measured force records with the aid of System Identification techniques, as carried out by Stansby *et al.* (1992) and Worden, Stansby & Tomlinson (1994) with reference to wave forces on a vertical cylinder. This work was based on an extension to Morison's equation to include Duffing oscillator-type force terms that involve the first and second rates of change of the force. The model was found to provide excellent agreement with measured force records, but was not very successful at predictions, when only the input (i.e. the kinematics of the flow) was known. A disadvantage of this type of approach is that the results cannot be related to physical processes, and therefore may not be robust, or able to be gracefully modified for different conditions. A related handicap is one simply of dimensions. If the kernel of a history force term were found from a set of measurements to be of the form $(t-\tau)^{-1/2}$ say, a group of dimensional parameters has to be found to relate the result to a force per unit length (for the cylinder problem). This can always be achieved by involving the viscosity (as in (2)), but at high Reynolds numbers there has to be an asymptotic form that is independent of the viscosity – in the same way that the drag on a bluff body ultimately becomes independent of the Reynolds number. This leaves only the kinematics of the problem – the velocity record and the cylinder's diameter – from which to construct the remainder of the history term. It seems unlikely that this could be done purely from the results of signal processing.

This paper sets out to adapt the asymptotic models of Hinch and Mei & Lawrence to the two-dimensional case of flow past a circular cylinder where prospects for analysis are hampered by the absence of counterparts of the Stokes and Basset solutions for steady and unsteady flow past a sphere. Uniquely, asymptotic models offer a rational approach to an understanding of history forces on a cylinder and they are therefore worth pursuing, even if, as seems likely from the outset (and is found to be the case), quantitative predictions are generally not very good except at very low Reynolds numbers. The results for several types of motion are compared with numerical solutions obtained with a time-stepping Navier–Stokes code that is described in § 3. Section 4 considers the elements of the steady-state wake, and § 5 considers the effects of impulsive changes in the incident flow. An asymptotic model is formulated that in § 6 is generalized to cover the case of a continuously changing incident flow. Agreement with numerical solutions is observed over a smaller range of conditions than in the case of a sphere.

3. The Navier–Stokes code

The Navier–Stokes code used in the present work is basically similar to that described in Chaplin (1993), using a finite difference spectral method to solve for the

stream function $\psi(r,\theta,t)$ and vorticity $\omega(r,\theta,t)$ with

$$\frac{\partial\omega}{\partial t}+\frac{1}{r}\left(\frac{\partial\psi}{\partial\theta}\frac{\partial\omega}{\partial r}-\frac{\partial\psi}{\partial r}\frac{\partial\omega}{\partial\theta}\right)=\frac{2}{Re}\nabla^2\omega, \tag{3}$$

$$\omega=-\nabla^2\psi, \tag{4}$$

where (r,θ) are cylindrical coordinates centred on the cylinder, and velocity components are $v_r=(1/r)\partial\psi/\partial\theta, v_\theta=-\partial\psi/\partial r$. All quantities are normalized by taking the cylinder's radius c, the speed of a reference incident flow $\hat{U}$, and $\rho\hat{U}^2$ as length, velocity, and stress scales, and $Re=2\hat{U}c/v$. To achieve a helpful distribution of mesh points in the radial direction, the computation is carried out on a mesh on the (x_1,θ)-plane, where the mapping between r and x_1 is (Mei 1993)

$$r=1+(r_E-1)\{1-c_r\tan^{-1}[(1-x_1)\tan(1/c_r)]\}. \tag{5}$$

On the cylinder's surface, $r=1, x_1=0$, and at the outer limit of the circular computational domain, $r=r_{\mathrm{E}}, x_1=1$. Finite difference mesh points are located at equal increments δx_1 in x_1, and their distribution in r is determined by the factor c_r which was set to 0.642 as in comparable cases in Mei (1993). The transformation (5) is more efficient than the exponential expansion $r=\exp x_1$ at providing a suitably high resolution close to the cylinder at the same time as a large value of r_E.

The stream function and vorticity are expanded in terms of spatial frequency components:

$$\psi(x_1,\theta,t)=\sum_{j=1}^{J}g_j(x_1,t)\sin j\theta, \tag{6}$$

$$\omega(x_1,\theta,t)=-\sum_{j=1}^{J}G_j(x_1,t)\sin j\theta, \tag{7}$$

imposing the restraint that the flow remains symmetrical about $\theta=0$. The substitution of (6) and (7) into (3) produces a formula for the time derivative by which the stream function coefficients $g_{i,j}$ can be updated from time level t to time level $t+\delta t$. This is applied in a fully centred implicit iterative Crank–Nicholson scheme at each time step. The boundary conditions for the stream function are provided by $\psi=0$ on $r=1$, and $\partial\psi/\partial r=rU\cos\theta$ on $r=r_E$ where U is the normalized instantaneous incident flow, and those for the vorticity are obtained by a Woods condition on the cylinder, and by putting $\omega(x_1=1)=\omega(x_1=1-\delta x_1)$. In the solutions described below the parameters $(r_E,\delta x_1,J,\delta t)$ were (1200, 1/100, 40, 0.005), (1200, 1/257, 75, 0.005), (1200, 1/257, 150, 0.005) for $Re=2,10,40$ respectively, except during ramped changes of velocity when $\delta t=0.0005$. Convergence tests were carried out at $Re=40$. For cases in which the outer radius was halved (600, 1/129, 150, 0.005), the radial resolution was halved (1200, 1/129, 150, 0.005), the number of frequencies was halved (1200, 1/257, 75, 0.005), or the time step was doubled (1200, 1/257, 150, 0.01), the effect on the drag at $t=250$ was less than 0.7%.

The force on the cylinder is the sum of shear and pressure contributions, and can be derived directly from the fundamental frequency components of the vorticity and of the radial vorticity gradient at the cylinder's surface. The drag coefficient is given by

$$C_d=\frac{2\pi}{Re}(G_1(0,t)-G_1'(0,t)), \tag{8}$$

	C_d			
Re	in Zdravkovich (1997)	Dennis & Chang (1970)	Fornberg (1980)	Present work
1	10.28			
2	6.637			6.649
4	4.437			
6	3.565			
7	3.291	3.421		
10	2.754	2.846		2.752
15	2.266			
20	2.003	2.045	2.000	
40	1.536	1.522	1.498	1.491
100		1.056	1.058	

TABLE 1. Drag coefficients for steady symmetrical flow past a cylinder.

and for this purpose the radial gradient of G_1 was estimated by a fourth-order forward difference formula.

Computed steady-state drag coefficients are shown in table 1, with some others from the literature, including results of Keller & Takami (1960), Keller (1958), Takami & Keller (1969) and Nieuwstadt & Keller (1973) summarized by Zdravkovich (1997, table 8.2). The latter are in good agreement with the present data at $Re = 2$ and 10, while at $Re = 40$ a better match is observed with computations by Fornberg (1980), who also reviewed drag coefficients from several other sources. In analysis presented later it is helpful to be able to express C_d as a continuous function of Re that passes through the present results, and for this purpose additional values were taken from those cited by Zdravkovich up to $Re = 20$, and those of Fornberg from $Re = 20$ to 100. These data provided a consistent set to which a curve could be fitted as described below.

Lamb's theory for a cylinder in creeping flow (Batchelor 1967, p. 246) gives

$$C_d = 8\pi/[Re\ln(7.4/Re)]. \tag{9}$$

At $Re = 0.01$ this meets, and has a common tangent with, $C_d = 7.638\ Re^{-0.849}$. For present purposes, reference drag coefficients will be determined from (9) for $Re < 0.01$, and

$$C_d(Re) = 7.638\,Re^{-0.849}\exp[0.0400\log^3(Re/0.01) - 0.000611\log^5(Re/0.01)] \tag{10}$$

for $Re > 0.01$. This is a close fit to the present data and those mentioned above.

In computing impulsive changes in fluid motion over solid boundaries it is necessary to give careful attention to the singular nature of the initial flow, and for this reason it would be wrong to model an impulsive start by simply applying the boundary condition $U = 0\,(t < 0), U = 1\,(t \geqslant 0)$ in the numerical scheme outlined above. As pointed out by Collins & Dennis (1973) this would ignore the boundary layer structure of the flow, and whatever the resolution of the finite difference solution, it will not be able to capture the starting motion. A correct approach (described by Collins & Dennis) is to start the solution on an expanding mesh with a scale $r \sim 2\sqrt{2t/Re}x_1$, and then switch over to a fixed mesh after the first few time steps. This technique was followed here for the validation exercise described below, but otherwise rapid changes in velocity were more conveniently imposed over a finite time interval Δt, following a

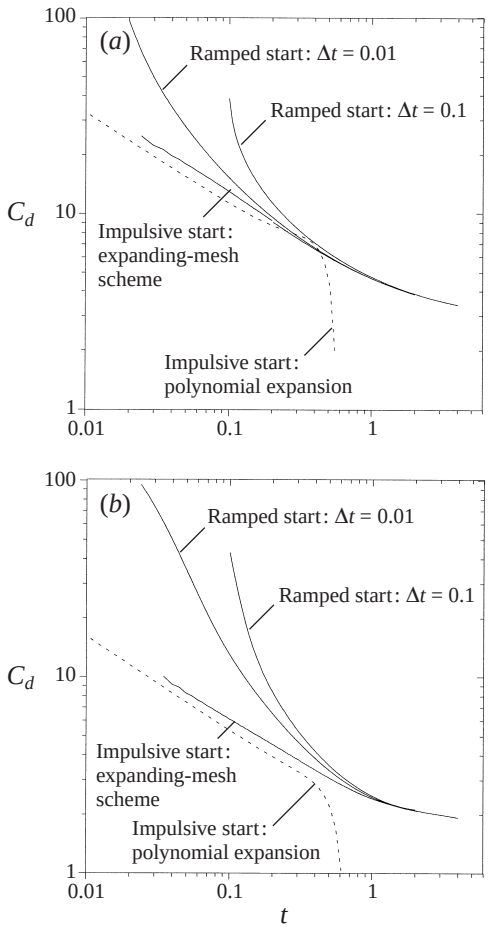

FIGURE 1. The drag coefficient of a cylinder following ramped and impulsive starts at (*a*) $Re = 10$ and (*b*) 40. Computation of the ramped starts followed the method of § 3, with initial velocity histories defined by equation (11) with $U_1 = 0$, $U_2 = 1$, and $\Delta t = 0.01$ or 0.1. Results for impulsive starts that are shown as continuous lines were obtained with a separate code based on the expanding-mesh scheme of Collins & Dennis (1973). Those shown as broken lines were computed directly from the polynomial expansion given by Collins & Dennis (1971).

smooth ramp of the form

$$U = U_1 + (U_2 - U_1)\sin^2\left(\frac{\pi t}{2\Delta t}\right). \tag{11}$$

It seems reasonable to expect that with $\Delta t = 0.01$ or 0.1, the flow after times of order 1 would be essentially the same as that following a truly impulsive change. As a test of this, figure 1 compares computed drag coefficients following ramped starts using equation (11) with $U_1 = 0, U_2 = 1$, with those obtained from a numerical solution using the expanding mesh scheme of Collins & Dennis (1973). Agreement is very close from about $t = 1$ suggesting that no serious inconsistencies will follow from the assumption that after this time interval, such ramped and impulsively changed flows would be essentially the same. The analytical solution for an impulsive start by Collins & Dennis (1971, equations (80) and (81)) is also shown in figure 1 as a

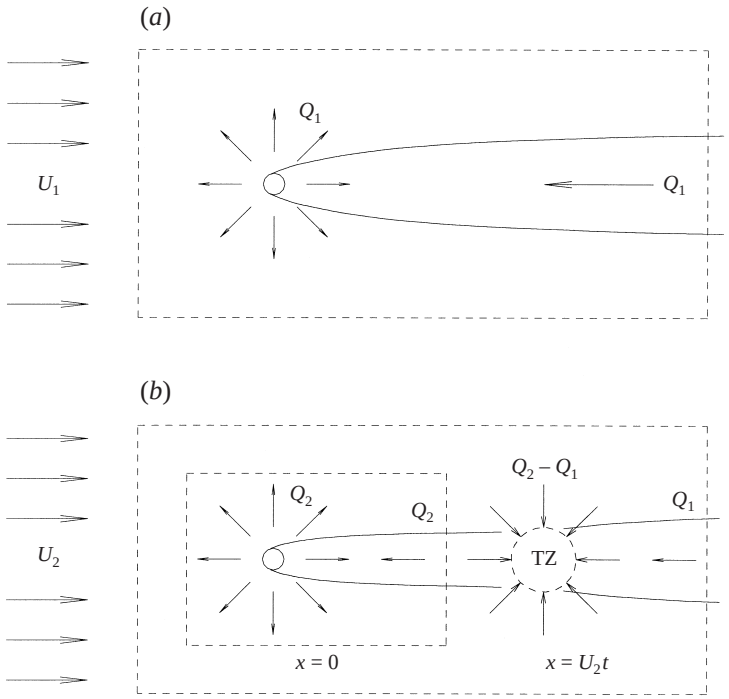

FIGURE 2. The structure of the flow (*a*) before and (*b*) after an impulsive change in the speed of the incident flow from U_1 to U_2. The corresponding wake fluxes are given by equation (13).

broken line for each Reynolds number. This is valid up to $t \sim 0.5$ for high Reynolds numbers but is evidently significantly in error for those as low as 10 and 40.

4. The steady-state wake

Consider first the dominant features of a steady-state wake behind a cylinder in a steady flow. Length and velocity scales are defined as $\hat{U}$ and c, as in § 3. The normalized streamwise velocity at a point x downstream from the cylinder is $U + u(x, y)$, where U is the speed of the incident flow, and within the central region of the wake $u < 0$. This reduction in the flow out of a large control volume surrounding the cylinder (shown in figure 2*a*) tends to a constant at large x, defined as

$$Q = -\int_{-\infty}^{\infty} u(y)\mathrm{d}y, \tag{12}$$

and is balanced by a flow that appears at large distances to be due to an irrotational source of the same strength at the cylinder. The dominant components in the integral momentum equation applied to a control volume that cuts the wake a large distance downstream are those that represent the rate of change of momentum and the drag (Batchelor 1967, p. 351). In dimensionless terms this implies

$$Q = C_d U \tag{13}$$

for $x \gg 1$, or $x = X/\varepsilon$ where ε is a small parameter and X is $O(1)$. A limiting form for the streamwise flow in the steady state wake (Batchelor 1967, p. 349) can be written

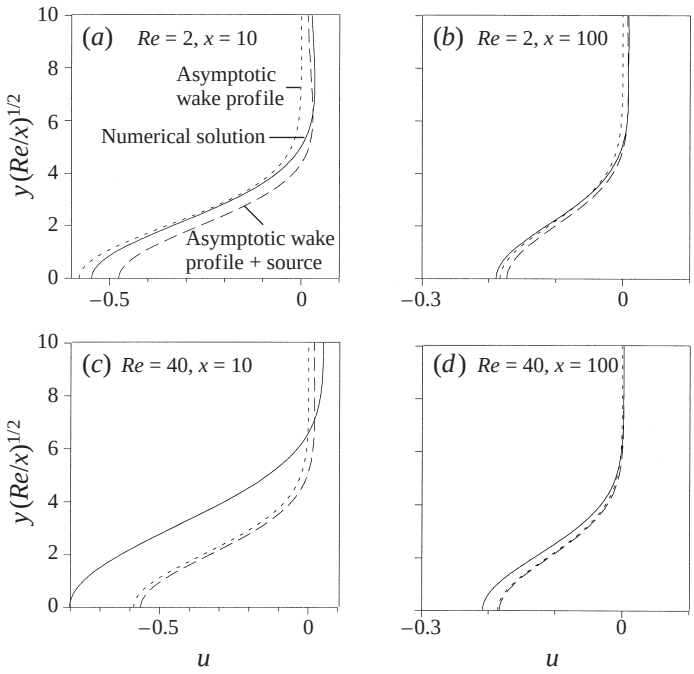

FIGURE 3. Streamwise velocity profiles across the steady-state wake. The asymptotic profile (14) is compared with results of the Navier–Stokes code at $t = 500$ after the start. A second broken line shows the combination of (14) with a source of strength Q (given by (13)) at the cylinder.

as

$$u = -C_d\sqrt{\frac{Re}{8\pi x}}\exp\left(-\frac{y^2 Re}{8x}\right). \tag{14}$$

As a preliminary to carrying out a similar exercise for the case of an unsteady wake, we consider the conditions under which (14) is valid, starting with the normalized steady-state vorticity transport equation

$$(U+u)\frac{\partial\omega}{\partial x} + v\frac{\partial\omega}{\partial y} = \frac{2}{Re}\left(\frac{\partial^2\omega}{\partial x^2} + \frac{\partial^2\omega}{\partial y^2}\right). \tag{15}$$

This equation may be re-scaled by putting $x = X/\varepsilon$, $y = Y/\sqrt{\varepsilon Re}$, $u = \hat{u}C_d\sqrt{\varepsilon Re}$, $v = \hat{v}C_d\varepsilon$ and $\omega = \hat{\omega}C_d\varepsilon Re$, where $Y, \hat{u}, \hat{v}$ and $\hat{\omega}$ are all expected to be $O(1)$. The result is

$$U\frac{\partial\hat{\omega}}{\partial X} + C_{\mathrm{d}}\sqrt{\varepsilon Re}\left(\hat{u}\frac{\partial\hat{\omega}}{\partial X} + \hat{v}\frac{\partial\hat{\omega}}{\partial Y}\right) = \frac{\epsilon}{Re}\frac{\partial^2\hat{\omega}}{\partial X^2} + \frac{\partial^2\hat{\omega}}{\partial Y^2}, \tag{16}$$

which can be approximated as $U\partial\hat{\omega}/\partial X = \partial^2\hat{\omega}/\partial Y^2$ when $C_d\sqrt{\varepsilon Re} \ll 1$ and $\varepsilon/Re \ll 1$. The corresponding solution for the streamwise velocity is then (14). Both inequalities are satisfied when $x \gg 1/Re$ (in conditions where (9) applies), or when $x \gg Re$ (at higher Reynolds numbers where C_d is $O(1)$).

The profile (14) is plotted across the wake in figure 3 at $x = 10$ and 100, at $Re = 2$ and 40, and compared with the results of the Navier–Stokes code at $t = 500$, by which time conditions at these sections had become essentially steady. Also shown is the result of a combination of (14) and a source of strength Q (from 13)) located

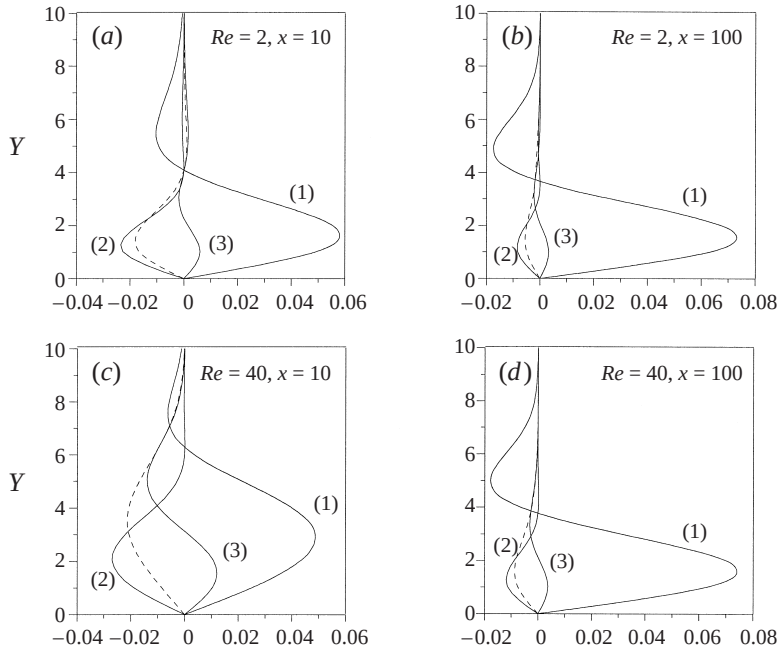

FIGURE 4. Terms on the left-hand side of equation (16) evaluated at sections across the wake. Lines denoted (1), (2) and (3) refer to the terms $U\,\partial\hat{\omega}/\partial X$, $C_d\sqrt{\varepsilon Re}\,\hat{u}\,\partial\hat{\omega}/\partial X$ and $C_d\sqrt{\varepsilon Re}\,\hat{v}\,\partial\hat{\omega}/\partial Y$ respectively. These results were computed from the Navier–Stokes code at $t = 500$ after the start. The broken lines represent the sum of terms (2) and (3) at each elevation Y.

at the cylinder. As expected, agreement between numerical and asymptotic solutions improves with x and deteriorates with Re.

At $x = 100$ the results are perhaps closer than might be anticipated from the corresponding values of the factor $C_d\sqrt{\varepsilon Re}$ in the left-hand side of (16)–about 0.9 at both Reynolds numbers. To see the reason for this, the contribution of each term on the left-hand side of (16) is shown in figure 4 for the same conditions as in figure 3, having been obtained from numerical solutions and scaled as described above, with $\varepsilon = 1/x$. The importance of the terms $u\partial\omega/\partial x$ and $v\partial\omega/\partial y$ in (15) is evidently reduced first by the fact that they are predominantly of opposite signs. Secondly, in proportion to $U\partial\omega/\partial x$, their magnitudes are smaller than those indicated by the re-scaling, presumably because of the presence of multipliers that are significantly different from unity. According to the approximate solution (14), $\hat{u}$ is about $1/\sqrt{8\pi} = 0.2$, and $U\partial\hat{\omega}/\partial X$ is in the region of $(3/32)\sqrt{2/\pi} = 0.075$. These results suggest that the consequences of simplifying (15) as described above may, in some respects, be less restrictive than indicated by the formal analysis.

Nevertheless, at Reynolds numbers above about 1, the near wake is influenced by strong shear layers which maintain a large reverse flow on the axis. Figure 5 shows wake centreline velocities at $Re = 2, 10$ and 40 obtained from the Navier–Stokes code at $t = 500$. These are compared with the sum of the wake profile (14) and a source of strength Q at the cylinder. To obtain a reasonable match with the numerical results while satisfying the boundary condition on the rear face of the cylinder ($u = -1$ at $x = 1$), both the origin of the wake and the position of the source were shifted from the centre of the cylinder. The source was placed at $x = 0.3$ in each case, and the origin of the wake was at $x = 0.454, -0.097$ and -0.970 at $Re = 2, 10$

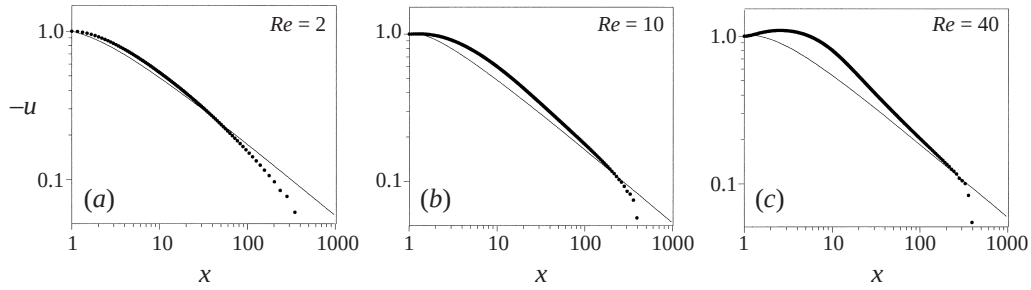

FIGURE 5. Wake centreline velocities. The lines are computed from the asymptotic wake profile (14) combined with a source at the cylinder. The locations of the origin of the wake and the source are given in the text. The points are from results of the Navier–Stokes code at $t = 500$ after the start.

and 40 respectively. Agreement with the numerical results deteriorates with increasing Reynolds number, and could not be improved significantly by any other choice of the location of the source or wake.

Much better agreement at all points in the steady wake was found by Mei & Lawrence (1996) for the case of a sphere at Reynolds numbers in the range 1 to 100. This can be associated with the fact that in the three-dimensional case the wake Reynolds number (formed from the centreline velocity and the wake width) decays as $x^{-1/2}$, whereas in the two-dimensional case it remains constant. Nevertheless, the asymptotic approach seems to provide a worthwhile starting point for a simple model of wake flow of a cylinder in unsteady conditions, as developed below.

5. Effects of an impulsive change in the incident flow

This Section follows the arguments in Hinch (1993) and Mei & Lawrence (1996) to identify the global features of the flow around a cylinder that experiences a single impulsive change in the incident velocity. Comparisons are made with predictions of the Navier–Stokes code described in § 3. Consider first the case of a cylinder in a flow whose velocity at $t = 0$ impulsively changes from $U_1 \geqslant 0$ to $U_2 > 0$. Before the change the flow is fully developed and its structure is as shown in figure 2(*a*), and $Q_1 = C_{d1} U_1 c$, where C_{d1} is the drag coefficient corresponding to the Reynolds number $2U_1 c/\nu$. After the change, there must exist a transition zone between the old and new wakes at $x = U_2 t$. Upstream of the transition zone there is a reversed flow of Q_2, and downstream one of Q_1. If $Q_2 > Q_1$ (corresponding to an increase in ambient velocity), the balance must be supplied by an inflow to the transition zone that at large distances appears as a sink of strength $Q_2 - Q_1$ located there, as shown in figure 2(*b*). The origin of the old wake (to the right of the transition zone), stationary when the incident flow was U_1, now moves with velocity $U_2 - U_1$.

When seen from a reference frame moving with velocity U_2, the flow in the region of the transition zone can be considered as the sum of one part which is associated with the asymptotic profiles of the old and new wakes to the right and left, and an second part (whose length and velocity scales are isotropic) associated with the diffusing transition zone between them. The streamwise velocity components of both must have similar magnitudes, so the total can be written $u = (\hat{u} + \hat{u}')C_d\sqrt{\varepsilon Re}$, where $\hat{u}'$ represents the part due to the transition zone. Similarly, the transverse velocity is now $v = \hat{v} C_d \varepsilon + \hat{v}' C_d \sqrt{\varepsilon Re}$. The length and time scales of the flow in the transition

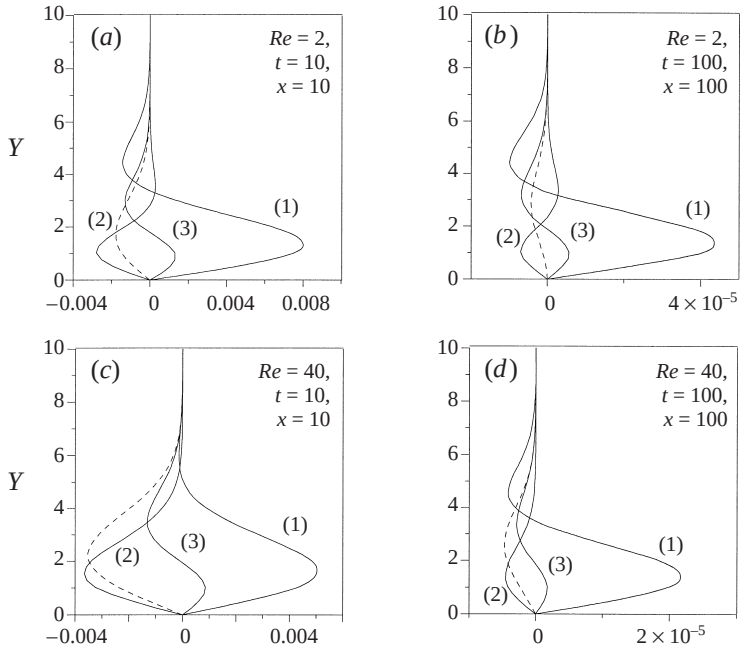

FIGURE 6. Values of each of the three terms on the left-hand side of the vorticity transport equation $\frac{\partial\omega}{\partial t}+u\frac{\partial\omega}{\partial x}+v\frac{\partial\omega}{\partial y}=\frac{2}{Re}\left(\frac{\partial^2\omega}{\partial x^2}+\frac{\partial^2\omega}{\partial y^2}\right)$ for a reference frame travelling with the ambient flow, (computed from results of the Navier–Stokes code and labelled (1), (2), (3) respectively) are plotted across the wake through the centre of the transition zone $x=t$, where t is the elapsed time since the flow started from rest. The broken lines represent the sum of terms (2) and (3) at each elevation Y.

zone are $(\varepsilon Re)^{-1/2}$ and ε^{-1}, and scaled coordinates are accordingly introduced by $x'=\xi/\sqrt{\varepsilon Re}$, $y=\eta/\sqrt{\varepsilon Re}$, $\omega=\hat{\omega}'C_d\varepsilon Re$, and $t=T/\varepsilon$, where $x'=x-U_2t$.

On substituting into the vorticity transport equation, and removing the terms on the left- and right-hand sides identical to those in (16), what remains is

$$\frac{\partial\hat{\omega}'}{\partial T}+C_d\sqrt{\varepsilon Re}\left(\hat{u}'\frac{\partial\hat{\omega}}{\partial X}+\hat{v}\frac{\partial\hat{\omega}'}{\partial\eta}\right)+C_dRe\left(\hat{u}\frac{\partial\hat{\omega}'}{\partial\xi}+\hat{u}'\frac{\partial\hat{\omega}'}{\partial\xi}+\hat{v}'\frac{\partial\hat{\omega}}{\partial Y}+\hat{v}'\frac{\partial\hat{\omega}'}{\partial\eta}\right)=\frac{\partial^2\hat{\omega}'}{\partial\xi^2}+\frac{\partial^2\hat{\omega}'}{\partial\eta^2}. \quad (17)$$

The second term on the left-hand side can be neglected under conditions mentioned previously, but it appears that no such arguments will support discarding the third term. In this respect the two-dimensional case differs from the axisymmetrical one (Mei & Lawrence 1996) in which, under certain conditions, all the convective terms can formally be shown to be negligible.

However (as in the steady state), the numerical importance of the convective terms in the present case may be less than that suggested by (17) (see figure 6), and it is worth exploring the validity of predictions for the unsteady wake based on the linearized vorticity transport equation

$$\frac{\partial\omega}{\partial t}=\frac{2}{Re}\left(\frac{\partial^2\omega}{\partial x^2}+\frac{\partial^2\omega}{\partial y^2}\right) \quad (18)$$

(applied on a reference frame moving with the ambient flow), with boundary condi-

tions to match the asymptotic wake profiles on either side. The solution is derived in the Appendix, leading to the following equation (obtained from the first two terms on the right-hand sides of (A 15) and (A 16)) for the streamwise velocity at an arbitrary point (x, y) due to the transition zone at $x = U_2 t$:

$$u_z(x,y,t) = (Q_2 - Q_1)\left\{ \frac{x'}{2\pi(x'^2 + y^2)} \left[\exp\left(\frac{-(x'^2 + y^2)}{4\nu t} \right) - 1 \right] + \frac{\mathrm{erf}(x'/2\sqrt{\nu t}) - \mathrm{sgn}(x')}{4\sqrt{\pi \nu t}} \exp\left(\frac{-y^2}{4\nu t} \right) \right\}, \tag{19}$$

where $\mathrm{sgn}(x) = x/|x|$.

There are two other contributions to the streamwise velocity at an arbitrary point. The first is provided by the asymptotic wake profile on either side of the transition zone

$$u_w(x,y,t) = -Q_2 \sqrt{\frac{U_2}{4\pi \nu x}} \exp\left(-\frac{U_2 y^2}{4\nu x} \right) \quad \text{for} \quad 0 < x < U_2 t, \tag{20}$$

$$u_w(x,y,t) = -Q_1 \sqrt{\frac{U_1}{4\pi \nu [x - (U_2 - U_1)t]}} \exp\left(-\frac{U_1 y^2}{4\nu [x - (U_2 - U_1)t]} \right) \quad \text{for} \quad x > U_2 t. \tag{21}$$

(When u_w is added to u_z, velocity discontinuities at $x = U_2 t$ are eliminated.) The final contribution is the effect of the source at the cylinder

$$u_s(x,y,t) = \frac{Q_2 x}{2\pi(x^2 + y^2)}. \tag{22}$$

At the centre of the transition zone $x = U_2 t$, approached in either direction, the streamwise flow is just the average of those due to the wakes on each side:

$$u_z(U_2 t, y, t) + u_w(U_2 t, y, t) = -\frac{Q_1 + Q_2}{4\sqrt{\pi \nu t}} \exp(-y^2/4\nu t). \tag{23}$$

The start

Following an impulsive start ($U_1 = 0$), a global model for the flow consists of the transition zone at $x = U_2 t$, the asymptotic wake $0 < x < U_2 t$, and the source at the cylinder. The stream function can be obtained from (19–22) by integration, and figure 7 compares the resulting streamlines (after the incident flow has been subtracted) with those from the Navier–Stokes code at Reynolds numbers 2 and 40, at times 10 and 100 after an impulsive (or in the latter method, a ramped) start. As expected, agreement is better at $Re = 2$ than $Re = 40$, and it improves at large times and large radii. In figure 8, streamwise velocity profiles at $x = t$ (i.e. through the centre of the transition zone) are plotted for similar conditions, showing excellent agreement at $Re = 2$, $t = 100$, but a very poor match at $Re = 40$ for all times. Close to the cylinder, particularly at $Re = 40$, flow velocities are greater in the numerical solutions because of stronger recirculation in the near wake, as mentioned above. This is also seen in figure 9, which compares centreline velocities along the wake. In the region $0 < x < U_2 t$ the centreline velocity $-u$ in the model decays as $x^{-1/2}$, and for $x > U_2 t$ as x^{-2}, in accordance with the effect of a source at the cylinder and a sink at the transition zone. The locations of the source and the wake origin are the same as those in figure 5.

The force on the cylinder may be estimated from the asymptotic model on a

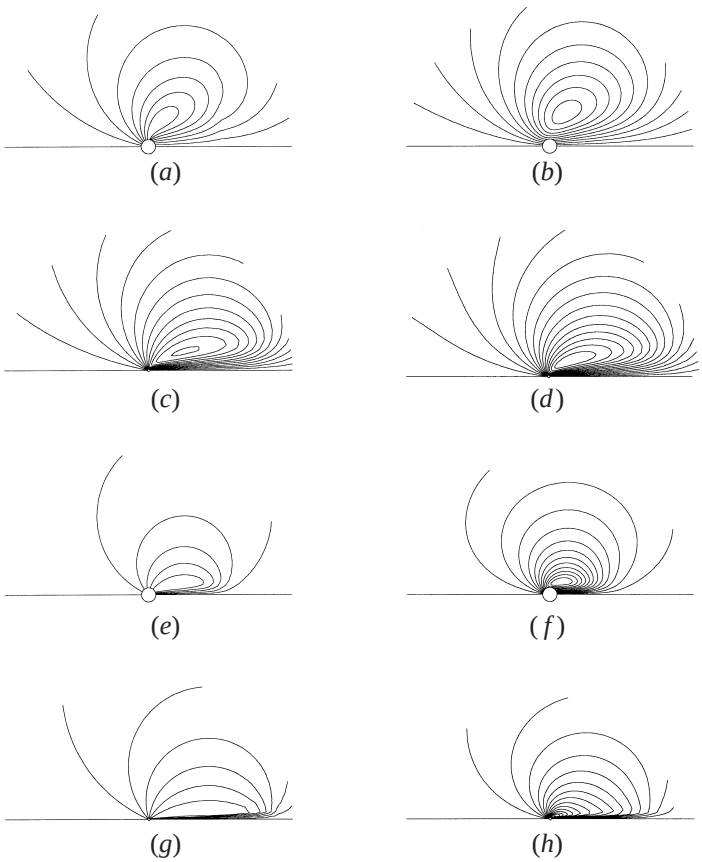

FIGURE 7. Instantaneous streamlines at time t after an impulsive start. Plots on the left are computed from the asymptotic model, those on the right from the Navier–Stokes code; (a, b) $Re = 2$, $t = 10$; (c, d) $Re = 2$, $t = 100$; (e, f), $Re = 40$, $t = 10$; (g, h) $Re = 40$, $t = 100$. The stream function interval is 0.2 in $(a$–$d)$, and 0.1 in $(e$–$h)$. The plots extend to a radius of 20 at $t = 10$, and 120 at $t = 100$. The undisturbed flow has been subtracted in all cases.

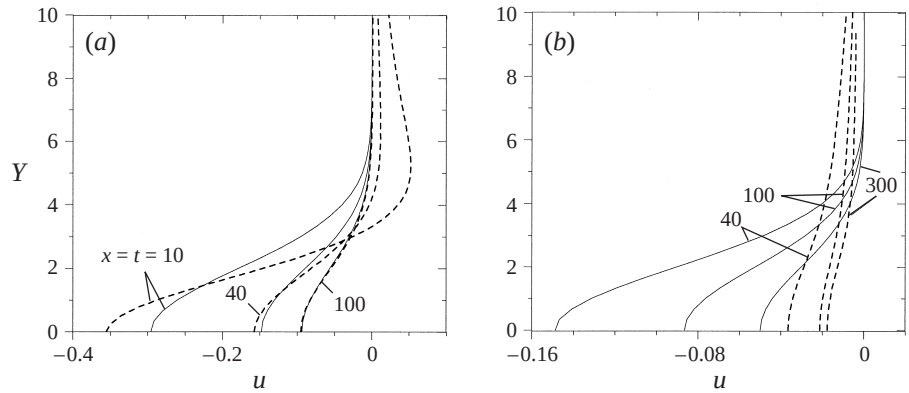

FIGURE 8. Instantaneous velocity profiles across the wake through the centre of the transition zone $x = t$, at various times t after the flow was started from rest: (a) $Re = 2$, (b) $Re = 40$. Solid lines were computed from the asymptotic model (23), broken lines from the Navier–Stokes code.

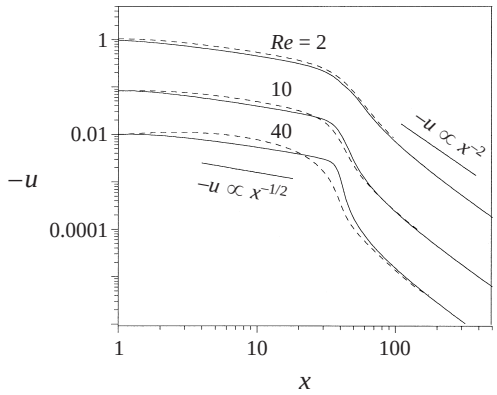

FIGURE 9. Wake centreline velocities at $t = 40$ after a start. Broken lines are from the Navier–Stokes code; full lines from the asymptotic model. Results for $Re = 10$ and 40 are shifted down by one and two decades respectively. The source at the cylinder and the wake origins are located as in figure 5.

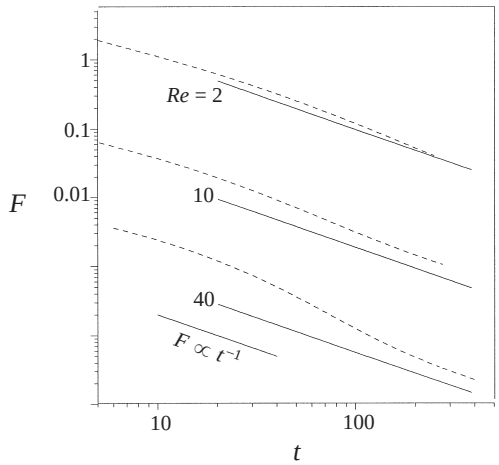

FIGURE 10. The transient part of the force on the cylinder at time t after the flow is impulsively started. Broken lines are from the Navier–Stokes code; full lines from the asymptotic model. Results for $Re = 10$ and 40 are shifted down by one and two decades respectively.

quasi-steady basis by considering the incident flow to be incremented by the velocity that the transition zone induces at the location of the centre of the cylinder. The instantaneous drag coefficient is similarly taken to be that corresponding to the Reynolds number $2[U_2 + u_z(0, 0, t)]c/\nu$. For large $U_2^2 t/4\nu$ the effect at the cylinder of the transition zone is predominantly that of a sink of strength Q_2 at $x = U_2 t$, and the resulting transient force decays ultimately as t^{-1}. This is consistent with the long-term behaviour of results for all Reynolds numbers as shown in figure 10, which plots the transient parts of the forces $F(t)$ obtained from the asymptotic model and from the Navier–Stokes code. At $Re = 2$ they become indistinguishable beyond $t = 250$, but at higher Reynolds numbers the asymptotic model clearly underestimates the unsteady part of flow in the wake (as seen for $Re = 40$ in figure 7).

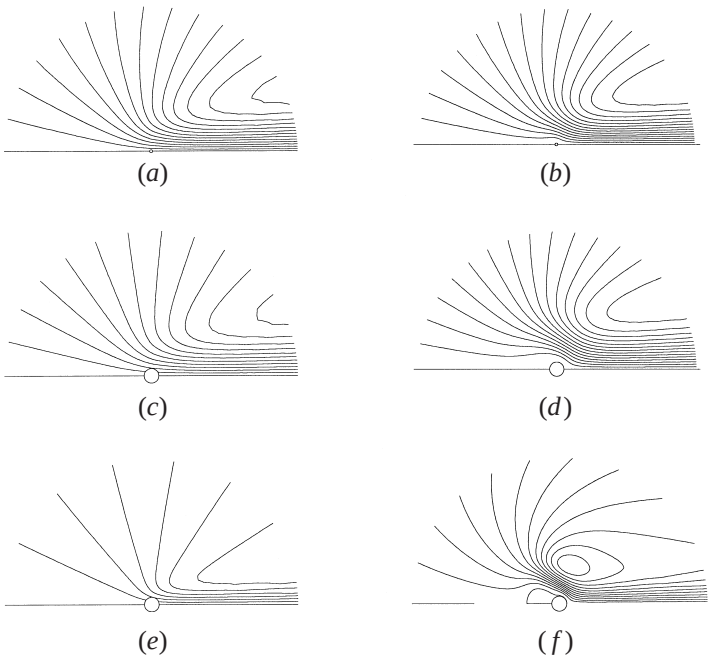

FIGURE 11. Streamlines at time t after an impulsive stop. Plots on the left are computed from the asymptotic model, those on the right from the Navier–Stokes code; (a, b) $Re = 2$, at $t = 100$; (c, d) $Re = 10$, and (e, f) $Re = 40$, both at $t = 20$. The stream function intervals are 0.2 at $Re = 2$, otherwise 0.1. The plots extend to a radius of 100 in (a, b), otherwise to a radius of 20.

The stop

After an impulsive stop ($U_2 = 0$) that occurs long after an impulsive start, the apparent origin of the old wake (previously at the cylinder) propagates to the left with speed U_1. The downstream end of the old wake (far to the right of the cylinder) is stationary. A second transition zone (containing a diffusing source) develops at the cylinder between the profile of the asymptotic wake on the right and the undisturbed fluid on the left. At the centre of this transition zone the net flow past the cylinder is one-half of that of the returning wake (which diffuses laterally), in accordance with (23). Streamlines computed on this basis for the flow after an impulsive stop are shown in the left hand column in figure 11. On the right are shown the corresponding results from the Navier–Stokes code. In this case the flow was stopped when it had run for 500 units of time after the initial start. Agreement between asymptotic and numerical models is very good at $Re = 2$, at $t = 100$ after the stop (figure 11a, b), but larger differences appear at earlier times and at higher Reynolds numbers. At $Re = 40$ a reverse wake appears in the numerical solution that cannot be captured by the asymptotic model (figure 11f).

The transient force may be calculated from the asymptotic model as described before, and figure 12 compares the results with those from the Navier–Stokes code. At large t, (23) and (9) point to $-F \propto 1/t^{1/2} \ln(t)$, and this is in agreement with the results, though in all cases the asymptotic model seriously under-estimates the magnitude of the transient force. A significant factor may be that in the model, the computation of the force neglects the considerable non-uniformity of the decaying ambient flow around the cylinder, shown in figure 11.

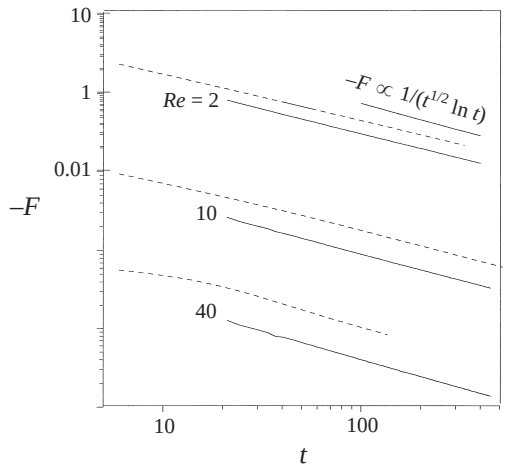

FIGURE 12. The force on the cylinder at time t after the flow is impulsively stopped. Broken lines are from the Navier–Stokes code, full lines from the asymptotic model. Results for $Re = 10$ and 40 are shifted down by one and two decades respectively.

The reverse

After an impulsive reverse ($U_2 < 0$) the flow that existed after the stop is convected to the left, and in addition a new wake is generated in that direction with a transition zone at its end (containing a diffusing sink). The elements of a global model therefore comprise the two superimposed transition zones at $x = U_2 t$ (where t is measured from the time of the reverse), a new wake $U_2 t < x < 0$ (with its origin at the cylinder and mass flux to the right), the old wake extending to the right from $x = U_2 t$ (with its apparent origin at $x = (U_2 - U_1)t$ and mass flux to the left), and a source at the cylinder.

Figure 13 compares streamline plots after a reverse with $U_2 = -U_1$ and similar remarks apply as before. In the model the strength of the growing wake to the left of the cylinder is attenuated by the fact that it is generated by the ambient flow alone, without any enhancement due to the old wake. The transient part of the force is plotted in figure 14, and in this case agreement with the numerical solution is better than for the start and the stop. As expected at large times $-F \propto 1/t^{1/2}$; the downturn at $t \sim 500$ results from the fact that the starting point in these calculations was the state of motion at 500 units of time after an impulsive start. It seems likely that agreement between asymptotic and numerical models in this case is improved fortuitously by the greater width of the downstream wake in the latter, and a consequent reduction in the velocity of the flow approaching the cylinder.

6. Arbitrary changes in the incident flow

The asymptotic model can be adapted to cover cases in which the ambient flow $U(t)$ is a continuous function of time. If the unsteadiness is represented as a series of step changes, the wake comprises a number of segments, each with a distinct reverse flux Q_i, as sketched in figure 15. The interface between the segments at each x_i reflects an earlier step change in the incident flow speed at time τ_i and is convected downstream with the ambient motion so that $x_i = \int_{\tau_i}^{t} U(\tau)\mathrm{d}\tau$. The ith wake segment has a self-induced velocity towards the cylinder of U_i, so that its apparent origin is at

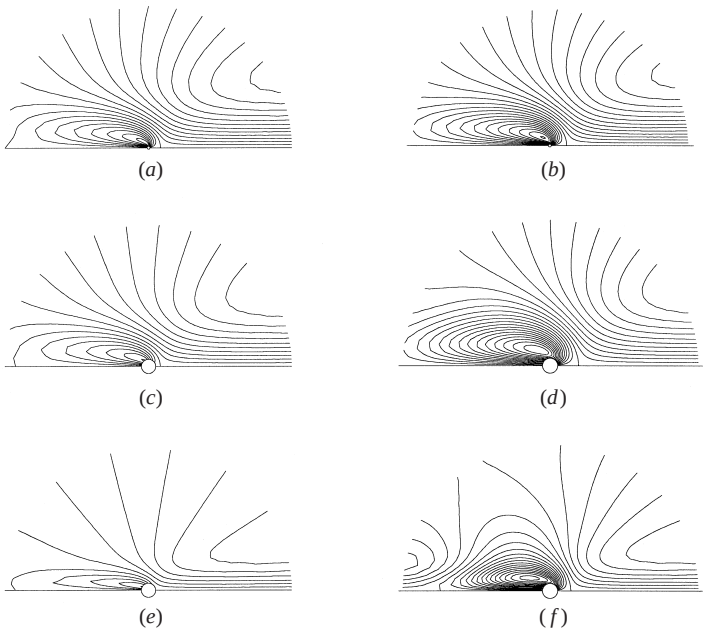

FIGURE 13. Streamlines at time t after an impulsive reverse. Plots on the left are computed from the asymptotic model, those on the right from the Navier–Stokes code; (a, b) $Re = 2$, at $t = 100$; (c, d) $Re = 10$, and (e, f) $Re = 40$, both at $t = 20$. The stream function intervals are 0.2 at $Re = 2$, otherwise 0.1. The plots extend to a radius of 100 in (a) and (b), otherwise to a radius of 20. The undisturbed flow has been subtracted in all cases.

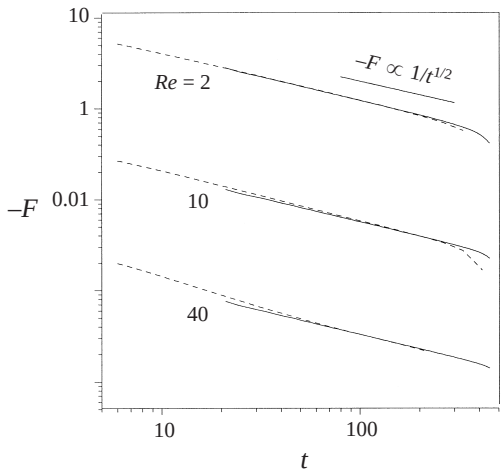

FIGURE 14. The transient part of the force on the cylinder at time t after the flow is impulsively reversed. Broken lines are from the Navier–Stokes code; full lines from the asymptotic model. Results for $Re = 10$ and 40 are shifted down by one and two decades respectively.

$x_i - U_i(t - \tau_i)$. The streamwise velocity at any point can be approximated as follows as the sum of the three contributions identified above.

Taking first the case of non-reversing flows $(U(t) > 0), (Q_2 - Q_1)$ in (19) may be replaced by $(\mathrm{d}Q/\mathrm{d}\tau)\mathrm{d}\tau$, leading to the following result for the streamwise velocity at a point (x, y) due to the non-uniformity of the wake (or in other words to the

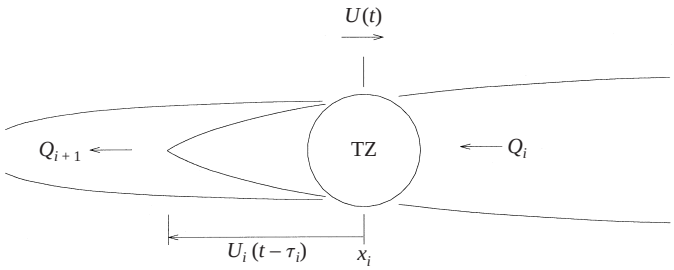

FIGURE 15. Elements of the unsteady flow around a transition zone. 'TZ' indicates the transition zone created by a step change in the flow speed from U_i to U_{i+1} at time τ_i.

distributed transition zones):

$$u_z(x,y,t) = \int_{-\infty}^{t} \frac{\mathrm{d}Q}{\mathrm{d}\tau} \left\{ \frac{x'}{2\pi(x'^2+y^2)} \left[\exp\left(\frac{-(x'^2+y^2)}{4\nu(t-\tau)} \right) - 1 \right] + \frac{\mathrm{erf}\,[x'/2\sqrt{\nu(t-\tau)}] - \mathrm{sgn}(x')}{4\sqrt{\pi\nu(t-\tau)}} \exp\left(\frac{-y^2}{4\nu(t-\tau)} \right) \right\} \mathrm{d}\tau, \tag{24}$$

where $x' = x - \int_{\tau}^{t} U(s)\mathrm{d}s$. There is also a contribution to the flow from the asymptotic wake profile at section x of

$$u_w(x,y,t) = -Q(\tau)\sqrt{\frac{1}{4\pi\nu(t-\tau)}} \exp\left(-\frac{y^2}{4\nu(t-\tau)} \right), \tag{25}$$

where τ is defined by $x = \int_{\tau}^{t} U(s)\mathrm{d}s$.

The final contribution is that of the source at the cylinder

$$u_s(x,y,t) = \frac{Q(t)x}{2\pi(x^2+y^2)}. \tag{26}$$

As each transition-zone element progresses downstream, its contribution to the velocity at the cylinder tends to that of a sink of corresponding strength, as noted above. Therefore the combined effect of the distributed transition zones is approximately

$$u_z(0,0,t) = \frac{1}{2\pi} \int_{-\infty}^{t} \left\{ \frac{\mathrm{d}Q}{\mathrm{d}\tau} \Big/ \int_{t-\tau}^{t} U(s)\mathrm{d}s \right\} \mathrm{d}\tau. \tag{27}$$

When the incident flow reverses, it is necessary to switch the sign of the integrand of (24). For the general case then

$$u_z(x,y,t) = \int_{-\infty}^{t} \mathrm{sgn}(U) \frac{\mathrm{d}Q}{\mathrm{d}\tau} \left\{ \frac{x'}{2\pi(x'^2+y^2)} \left[\exp\left(\frac{-(x'^2+y^2)}{4\nu(t-\tau)} \right) - 1 \right] + \frac{\mathrm{erf}\,[x'/2\sqrt{\nu(t-\tau)}] - \mathrm{sgn}(x')}{4\sqrt{\pi\nu(t-\tau)}} \exp\left(\frac{-y^2}{4\nu(t-\tau)} \right) \right\} \mathrm{d}\tau \tag{28}$$

and (22) has to be replaced by

$$u_w(x,y,t) = \sum_k -Q(\tau_k)\sqrt{\frac{1}{4\pi\nu(t-\tau_k)}} \exp\left(-\frac{y^2}{4\nu(t-\tau_k)} \right) \tag{29}$$

where the τ_k are the multiple solutions of $x = \int_{\tau}^{t} U(s)\mathrm{d}s$, up to a maximum of the

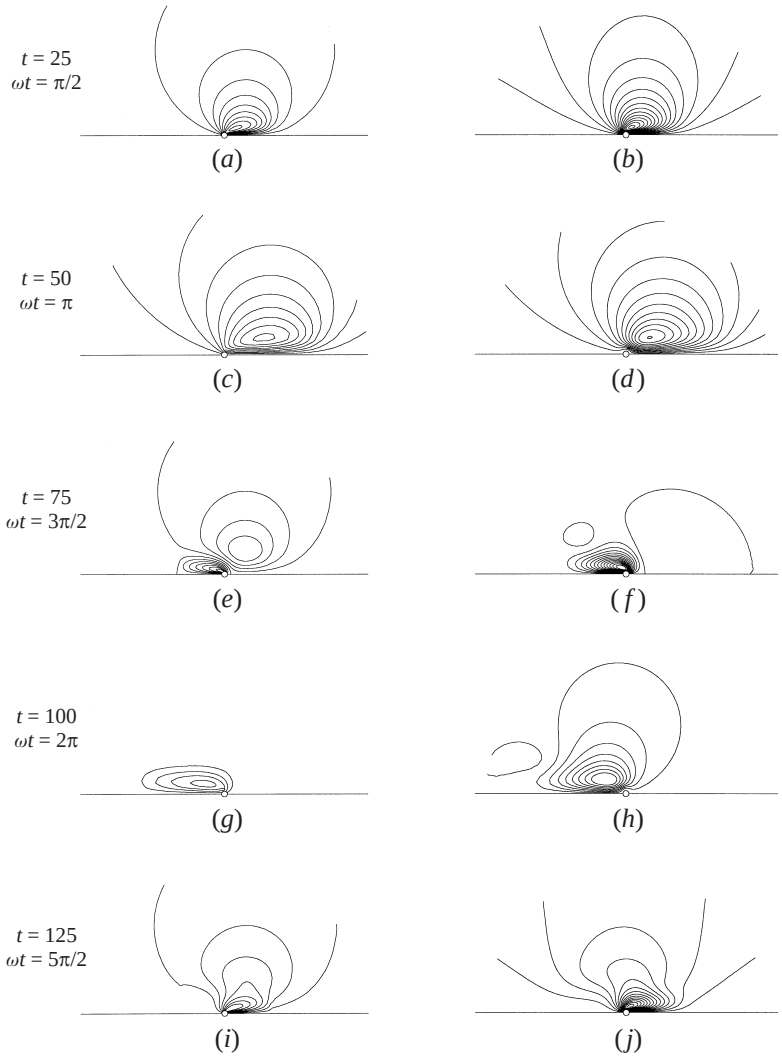

FIGURE 16. Instantaneous streamlines for oscillatory motion of amplitude $50/\pi$, maximum $Re = 10$. Plots on the left are computed from the asymptotic model, those on the right from the Navier–Stokes code. The stream function interval is 0.1, and the instantaneous incident flow has been subtracted in each case. The plots extend to a radius of 50.

number of times the flow has reversed. All the elements of the starting, stopped and reversed flows described in § 5 are captured by (28), (29) and (26).

In oscillatory flow, the conditions for which the model is best suited are likely to be those of large amplitudes, since the wake matches the asymptotic profile only at large distances from the cylinder. In figure 16, streamlines are shown at intervals of one-quarter of the period for an oscillatory ambient flow $U = \sin \omega t$ starting from rest with a displacement amplitude of $50/\pi$ cylinder radii (corresponding to a Keulegan–Carpenter number $K = 2\pi \times$ amplitude/diameter $= 50$) and a maximum Reynolds number of 10. The asymptotic model captures many features of the numerical solution, though as before the induced flow in the former is weaker.

The corresponding drag forces are plotted in figure 17(*a*). Besides the result from the asymptotic model, computed as described above, and that of the Navier–Stokes code,

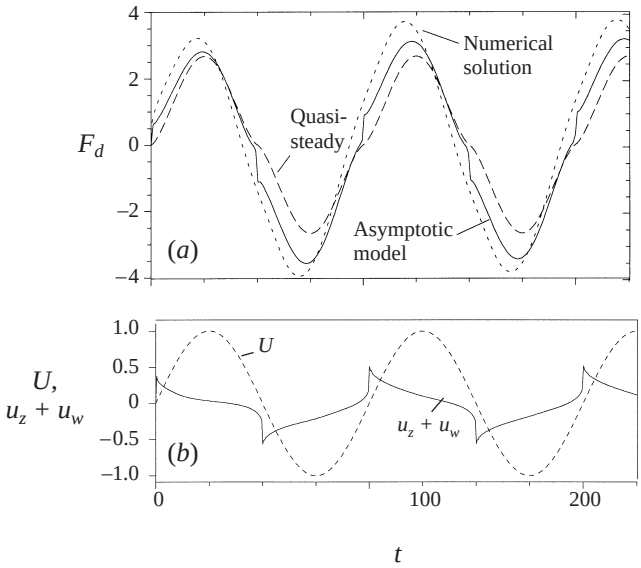

FIGURE 17. (*a*) The drag on the cylinder in an oscillatory flow starting from rest with a displacement amplitude of $50/\pi$ ($K = 50$), and maximum $Re = 10$. The results labelled 'quasi-steady' are computed from the instantaneous incident velocity and the corresponding steady-state drag coefficient; (*b*) the undisturbed incident velocity and the induced velocity at the cylinder.

from which the inertia force $2\pi\dot{U}$ was subtracted, figure 17(*a*) also shows the quasi-steady force obtained from the instantaneous velocity and the corresponding steady-state drag coefficient. The difference between this and the results of the asymptotic model is the history force.

When the incident velocity passes smoothly through zero, a rapid change occurs in the induced velocity predicted by the asymptotic model at the location of the cylinder's centre. The induced velocity is shown in figure 17(*b*) and the effect of the rapid change, which is caused by the newly generated wake being swept back upstream, is evident in the forces shown in figure 17(*a*). However, unlike the cases of impulsive changes to the incident flow, here there is no discontinuity in the induced velocity itself, and the force remains bounded at all times. The asymptotic model accounts for a large part of the difference between the numerical solution and the quasi-steady prediction.

7. Conclusions

An asymptotic model of unsteady rectilinear flow around a cylinder in the enforced absence of vortex shedding is compared with the results of numerical modelling at Reynolds numbers up to 40. Agreement is inferior to that found in the case of a sphere by Mei & Lawrence (1996), but nevertheless the model captures many features of the flow and the loading, and provides a basis from which history forces may be calculated. Following an impulsive start, stop and reverse, the transient part of the force decays ultimately as t^{-1}, $[t^{1/2}\log(t)]^{-1}$ and $t^{-1/2}$, respectively. In cases of oscillatory flow, the model correctly reproduces the characteristics of history forces that are generated by the cylinder encountering its own wake. Applications at higher Reynolds numbers would require some empirical intervention.

This work was carried out at the Department of Civil Engineering, University of British Columbia, Vancouver, with support from the Technology Foresight Award scheme of the Royal Academy of Engineering. The author is indebted to Michael Isaacson for helpful arrangements and discussions.

Appendix. Unsteady solution for the transition zone

Figure 2(*b*) shows the structure of the flow at a time t after a change in velocity from U_1 to U_2. The transition zone between the old wake and the new wake is at $x = U_2 t$, where x is measured from the origin of the new wake, a point assumed to be at the cylinder. The old wake was stationary when the incident flow speed was U_1, and so after the change it propagates downstream with velocity $U_2 - U_1$. The region to the left of the transition zone is dominated by the new wake, while that to the right is dominated by the old, whose origin is at $(U_2 - U_1)t$. Using a velocity profile of the form

$$U - Q\sqrt{\frac{U}{4\pi\nu x}}\exp\left(-\frac{Uy^2}{4\nu x}\right) \tag{A 1}$$

at a section in each wake x from its origin, the velocity on the left of the transition zone (relative to the incident flow U_2) is

$$u_{\mathrm{TZL}} = -\frac{Q_2}{2\sqrt{\pi\nu t}}\exp\left(-\frac{y^2}{4\nu t}\right) \tag{A 2}$$

while that on the right ($x = U_1 t$) is

$$u_{\mathrm{TZR}} = -\frac{Q_1}{2\sqrt{\pi\nu t}}\exp\left(-\frac{y^2}{4\nu t}\right). \tag{A 3}$$

It is seen that at the transition zone the old and new wakes have the same width, but that there is a difference in the flow rates of $Q_2 - Q_1$. We derive a solution for the two-dimensional matching flow (generally following the steps taken by Mei & Lawrence for the axisymmetric case), beginning with the linearized vorticity transport equation and shifting the origin of x to the centre of the transition zone,

$$\frac{\partial\omega}{\partial t} = \nu\left(\frac{\partial^2\omega}{\partial x^2} + \frac{\partial^2\omega}{\partial y^2}\right). \tag{A 4}$$

A vorticity distribution $\omega(x, y, t)$ is sought that satisfies (A 4) with boundary conditions to the left and right respectively

$$-\frac{Q_2 y}{4\sqrt{\pi(\nu t)^3}}\exp\left(-\frac{y^2}{4\nu t}\right) \quad \text{and} \quad -\frac{Q_1 y}{4\sqrt{\pi(\nu t)^3}}\exp\left(-\frac{y^2}{4\nu t}\right) \tag{A 5}$$

from (A 2) and (A 3). A solution of the form $\omega = f(y, t)g(x, t)$ implies

$$g\left(\nu\frac{\partial^2 f}{\partial y^2} - \frac{\partial f}{\partial t}\right) = f\left(\frac{\partial g}{\partial t} - \nu\frac{\partial^2 g}{\partial x^2}\right). \tag{A 6}$$

It is easily shown that

$$f = -\frac{y}{4\sqrt{\pi(\nu t)^3}}\exp\left(-\frac{y^2}{4\nu t}\right) \tag{A 7}$$

achieves a zero on the left-hand side of (A 6), and

$$g = Q_1 + \tfrac{1}{2}(Q_2 - Q_1)\,\mathrm{erfc}\left(\frac{x}{\sqrt{4\nu t}}\right) \tag{A 8}$$

achieves one on the right. From the vorticity $\omega = fg$ the next step is to calculate the velocity components and stream function. From the continuity equation and the definition of vorticity, it follows that

$$\frac{\partial \omega}{\partial x} = \frac{\partial^2 v}{\partial x^2} + \frac{\partial^2 v}{\partial y^2} \tag{A 9}$$

and from (A 7) and (A 8),

$$\frac{\partial \omega}{\partial x} = \frac{(Q_2 - Q_1)}{8(\nu t)^2} y \exp\left(-\frac{x^2 + y^2}{4\nu t}\right). \tag{A 10}$$

Equating the right-hand sides of (A 9) and (A 10) leads to a solution of the form

$$v = \frac{Q_2 - Q_1}{2\pi} \frac{y}{x^2 + y^2} \exp\left(-\frac{x^2 + y^2}{4\nu t}\right). \tag{A 11}$$

The definition of vorticity then leads to the following expression for u:

$$u = \frac{Q_2 - Q_1}{2\pi} \frac{x}{x^2 + y^2} \exp\left(-\frac{x^2 + y^2}{4\nu t}\right) - \frac{1}{2\sqrt{\pi \nu t}} \times \left[Q_1 + \tfrac{1}{2}(Q_2 - Q_1) \operatorname{erfc}\left(\frac{x}{2\sqrt{\nu t}}\right)\right] \exp\left(-\frac{y^2}{4\nu t}\right). \tag{A 12}$$

The right-hand sides in (A 11) and (A 12) reflect the presence of a singularity at the centre of the transition zone that can be removed by the addition of an irrotational sink there (while still satisfying the boundary conditions) of strength $Q_2 - Q_1$. The streamwise velocity component in the transition zone is then

$$u_{\mathrm{TZ}} = \frac{Q_2 - Q_1}{2\pi} \frac{x}{x^2 + y^2} \left\{\exp\left(-\frac{x^2 + y^2}{4\nu t}\right) - 1\right\} - \frac{1}{2\sqrt{\pi \nu t}} \left[Q_1 + \tfrac{1}{2}(Q_2 - Q_1) \operatorname{erfc}\left(\frac{x}{2\sqrt{\nu t}}\right)\right] \exp\left(-\frac{y^2}{4\nu t}\right) \tag{A 13}$$

(with a similar adjustment to (A 11)) from which it follows that the stream function is

$$\psi_{\mathrm{TZ}} = \frac{Q_2 - Q_1}{2\pi} \left\{\int_0^y \frac{x}{x^2 + y^2} \exp\left(-\frac{x^2 + y^2}{4\nu t}\right) \mathrm{d}y - \arctan\left(\frac{y}{x}\right)\right\} - \frac{1}{2}\left[Q_1 + \tfrac{1}{2}(Q_2 - Q_1) \operatorname{erfc}\left(\frac{x}{2\sqrt{\nu t}}\right)\right] \operatorname{erf}\left(\frac{y}{2\sqrt{\nu t}}\right), \tag{A 14}$$

making $\psi = 0$ on $y = 0$. The transition zone solution may be merged into the wakes to left and right by subtracting its limiting values (A 2) and (A 3) from (A 13), and adding the respective wake profile of the form (A 1). Thus for $x \leqslant 0$ and $x \geqslant 0$ the combined flows are respectively

$$u_{\mathrm{L}} = u_{\mathrm{TZ}} - u_{\mathrm{TZL}} - Q_2 \sqrt{\frac{U_2}{4\pi \nu (x + U_2 t)}} \exp\left(-\frac{U_2 y^2}{4\nu (x + U_2 t)}\right) \tag{A 15}$$

$$u_{\mathrm{R}} = u_{\mathrm{TZ}} - u_{\mathrm{TZR}} - Q_1 \sqrt{\frac{U_1}{4\pi \nu (x + U_1 t)}} \exp\left(-\frac{U_1 y^2}{4\nu (x + U_1 t)}\right). \tag{A 16}$$

REFERENCES

Basset, A. B. 1888 *A Treatise on Hydrodynamics*. Deighton Bell, London. Republished 1961 by Dover, New York.

Batchelor, G. K. 1967 *An Introduction to Fluid Dynamics*. Cambridge University Press.

Boussinesq, J. 1885*a Applications a l'Etude des Potentieles*. Reprinted 1969 by Blanchard, Paris.

Boussinesq, J. 1885*b* Sur la resistance qu'oppose un liquide indefini en repos...' *C. R. Acad. Sci. Paris* **100**, 935–937.

Chaplin, J. R. 1993 Orbital flow around a circular cylinder. Part 2. Attached flow at larger amplitudes. *J. Fluid Mech.* **246**, 397–418.

Collins, W. M. & Dennis, S. C. R. 1971 The initial flow past an impulsively started circular cylinder. *Q. J. Mech. Appl. Maths* **26**, 53–75.

Collins, W. M. & Dennis, S. C. R. 1973 Flow past an impulsively started circular cylinder. *J. Fluid Mech.* **60**, 105–127.

Dennis, S. C. R. & Chang, G.-Z. 1970 Numerical solutions for steady flow past a circular cylinder at Reynolds numbers up to 100. *J. Fluid Mech.* **42**, 471–489.

Fornberg, B. 1980 A numerical study of steady viscous flow past a circular cylinder. *J. Fluid Mech.* **98**, 819–855.

Hamilton, W. S. 1972 Fluid force on accelerating bodies. In *Proc. 13th Coastal Engng Conf., ASCE, New York*, vol. 3, pp. 1767–1782.

Hinch, E. J. 1993 The approach to steady state in Oseen flows. Appendix D in Lovalenti & Brady (1993).

Keller, H. B. 1958 On some iterative methods for solving elliptic difference equations *Q. Appl. Maths* **16**, 209–226.

Keller, H. B. & Takami, H. 1960 Numerical studies of steady viscous flow about cylinders. In *Numerical Solutions of Nonlinear Differential Equations* (ed. D. Greenspan). Wiley.

Lawrence, C. J. & Mei, R. 1995 Long term behaviour of the drag in impulsive motion. *J. Fluid Mech.* **283**, 307–327.

Lovalenti, P. M. & Brady, J. F. 1993 The hydrodynamic force on a rigid particle undergoing arbitrary time-dependent motion at small Reynolds numbers. *J. Fluid Mech.* **256**, 561–601.

Matsumoto, K. 1996 Prediction of hydrodynamic forces on oscillating bodies by unsteady turbulent wake theory. PhD thesis, Osaka University, Japan.

Mei, R. 1993 History force on a sphere due to a step change in the free-stream velocity. *Intl J. Multiphase Flow* **19**, 509–525.

Mei, R. 1994 Flow due to an oscillating sphere and an expression for unsteady drag on the sphere at finite Reynolds number. *J. Fluid Mech.* **270**, 133–174.

Mei, R. & Lawrence, C. J. 1996 The flow field due to a body in impulsive motion. *J. Fluid Mech.* **325**, 79–111.

Mei, R., Lawrence, C. J. & Adrian, R. J. 1991 Unsteady drag on a sphere at finite Reynolds number with small fluctuations in the free stream velocity. *J. Fluid Mech.* **233**, 613–628.

Michaelides, E. E. 1997 Review – the transient equation of motion for particles, bubbles and droplets. *Trans. ASME: J. Fluids Engng* **119**, 233–247.

Morison, J. R., O'Brien, M. P., Johnson, J. W. & Shaaf, S. A. 1950 The force exerted by surface waves on piles. *Petrol. Trans.* **189**, 149–154.

Nieuwstadt, F. & Keller, H. B. 1973 Viscous flow past circular cylinders. *J. Comput Fluids* **1**, 59–71.

Odar, F. & Hamilton, W. S. 1964 Forces on a sphere accelerating in a viscous fluid. *J. Fluid Mech.* **18**, 302–314.

Proudman, I. & Pearson, J. R. A. 1957 Expansions at small Reynolds numbers for the flow past a sphere and a circular cylinder. *J. Fluid Mech.* **2**, 237–262.

Sano, T. 1981 Unsteady flow past a sphere at low Reynolds number. *J. Fluid Mech.* **112**, 433–441.

Stansby, P. K., Worden, K., Tomlinson, G. R. & Billings, S. A. 1992 Improved wave force classification using system identification. *Appl. Ocean Res.* **14**, 107–118.

Takami, H. & Keller, H. B. 1969 Steady two-dimensional viscous flow of an incompressible fluid past a circular cylinder. *Phys. Fluids* **12**, 51–56.

Vojir, D. J. & Michaelides, E. E. 1994 Effect of history term on the motion of rigid spheres in a viscous fluid. *Intl J. Multiphase Flow* **20**, 547–556.

Worden, K., Stansby, P. K. & Tomlinson, G. R. 1994 Identification of nonlinear wave forces. *J. Fluids Struct.* **8**, 19–71.

Zdravkovich, M. M. 1997 *Flow Around Circular Cylinders: Vol. 1 Fundamentals.*. Oxford University Press.